Optics Letters

Observation of robust edge mode and in-gap corner mode in Kagome surface-wave photonic crystals

Ke Shen,[1] Wei-Min Deng,[1] Hao-Chang Mo,[1] Fu-Long Shi,[1] Fei Ma,[1,2] Xiao-Dong Chen,[1,2,*] and Jian-Wen Dong[1,2]

[1]School of Physics, Sun Yat-sen University, Guangzhou 510275, China
[2]State Key Laboratory of Optoelectronic Materials and Technologies, Sun Yat-sen University, Guangzhou 510275, China
*chenxd67@mail.sysu.edu.cn

Received 24 February 2023; revised 3 April 2023; accepted 21 April 2023; posted 21 April 2023; published 17 May 2023

Recent theory has demonstrated that Kagome photonic crystals (PCs) support first-order and second-order topological phenomena. Here, we extend the topological physics of the Kagome lattice to surface electromagnetic waves and experimentally show a Kagome surface-wave PC. Under the protection of first-order and second-order topologies, both robust edge modes and in-gap corner modes are observed. The robust transport of edge modes is demonstrated by high transmission through the waveguide with a sharp bend. The localized corner mode is found at the corner with one isolated rod when a triangle-shaped sample is constructed. Our work not only shows a platform to mimic the topological physics in classical wave systems, but also offers a potential application in designing high-performance photonic devices.

https://doi.org/10.1364/OL.488612

Photonic crystals (PCs) are periodic optical structures in which the electromagnetic waves propagate in a similar way as the electrons move inside the periodic potential of semiconductor crystals. By utilizing the passing bulk bands and forbidden bandgaps of PCs, many unusual photonic phenomena, such as super-prism dispersion [1], negative refraction [2], and sub-wavelength imaging [3] have been realized. Recently, with the introduction of topological photonics [4–7], different types of topological PCs have been proposed and realized [8–10]. For example, magnetic PCs with nonzero Chern numbers have been realized and one-way edge modes were observed [11–13]. For another example, spin-Hall PCs with nonzero spin Chern numbers have also been achieved and robust edge modes against disorders were demonstrated [14–18]. By using the topologically protected robust edge modes, high-performance photonic waveguides have been realized [19–21]. At first, the edge modes of topological PCs were found to be one dimension lower than the bulk. It was later revealed that there are other types of PCs with higher-order topological phases that do not obey the traditional bulk-edge correspondence [22–27]. For example, second-order two-dimensional (2D) PCs have zero-dimensional corner modes which are two dimensions lower than the bulk. By using the localized corner modes, nanophotonic cavities have been designed and fabricated [28,29]. Apart from the bulk PCs, surface-wave systems provide a unique platform to study topological physics. Surface-wave PCs are periodically textured metal surfaces which support spoof surface plasmons [30]. Many applications of surface-wave PCs have been demonstrated, such as optical cavities [31] and waveguides with sharp bends [32,33]. So far, topological states have been realized in many surface-wave systems, such as acoustic surface waves [34,35], 2D photonic surface waves [36–41], and even 3D topological materials [42].

Inspired by the recent development of first-order and second-order topological physics, Kagome PCs have been proposed to support both edge modes and corner modes. In this work, we extend the topological physics of the Kagome lattice to surface electromagnetic waves and experimentally show a Kagome surface-wave PC. Based on the breathing Kagome lattice, we numerically show and experimentally observe gapless and gapped bulk bands. Topological phase transition is achieved by controlling the strength of intracell and intercell couplings between neighboring metallic rods. By interfacing two topologically distinct PCs together, edge modes are observed and their robustness against a sharp bend is proved. In addition, the localized corner mode is also observed at the corners of the triangle-shaped sample.

The schematic of the unit cell and the top view of the considered Kagome surface-wave PC are shown in Fig. 1(a). It is a Kagome lattice of metallic rods standing on a metal surface. The structural parameters are the diameter of rod $d = 3.7$ mm, the height of rod $h = 14$ mm, and the lattice constant $a = 18.7$ mm. In the simulation, both the metallic rods and the substrate are considered as perfect electric conductors in the microwave region. Note that between the metallic rods and the metal surface, there is a homogeneous air spacer (effective thickness of 0.11 mm) because thin poster paper is placed for patterning the metallic rods during the experiment. Within the unit cell, there are three metallic rods which are symmetrically placed around the center of the unit cell. The distance between the center of the unit cell and the center of the rod is denoted as R. When $R = R_0 = \sqrt{3}a/6$, the distance between the intracell rods and the distance between the intercell rods are the same [inset of the middle panel of Fig. 1(c)]. This means that the intracell and intercell couplings between neighboring rods are the same, leading to degeneracy between the two bulk modes at the K point. This is confirmed by

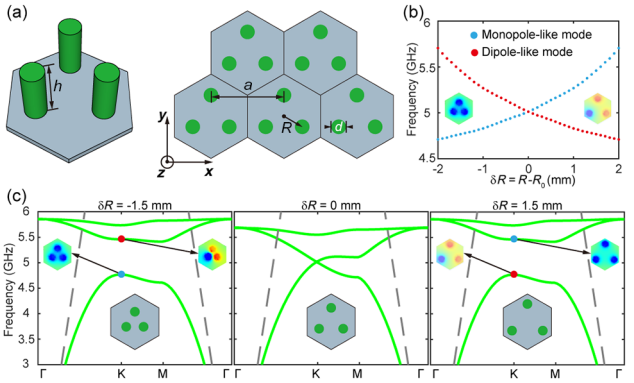

Fig. 1. Kagome surface-wave PC and its bulk bands. (a) The bird's-eye view of the unit cell and the top view of the Kagome surface-wave PC. Structural parameters: height of metallic rod (h), diameter of metallic rod (d), lattice constant (a), distance between the center of unit cell and the center of metallic rod (R). (b) Frequencies of two lowest bulk modes at the K point as a function of δR which is defined as $\delta R = R - R_0$. Insets: E_z fields at the xy plane which is 1 mm above the top of metallic rods for two bulk modes. (c) Bulk bands of three PCs with $\delta R = -1.5$ mm (left), $\delta R = 0$ (middle), and $\delta R = 1.5$ mm (right). Dashed gray lines denote the light line. Insets show the corresponding unit cells and E_z fields for the two bulk modes within the xy plane.

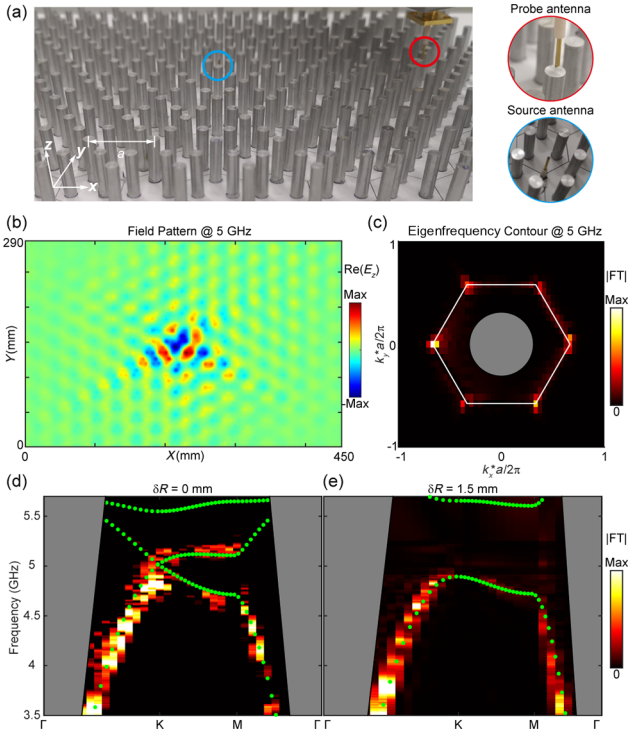

Fig. 2. Observation of gapless and gapped bulk bands. (a) Photograph of the Kagome surface-wave PC which consists of a Kagome lattice of aluminum rods standing on a flat aluminum surface. Zoom-in pictures of probe and source antenna are shown. (b) Measured E_z field at 5 GHz for the xy plane which is 1 mm above the top of metallic rods. (c) Measured eigenfrequency contour at 5 GHz for the PC with $\delta R = 0$ mm. (d) Measured gapless bulk bands for the PC with $\delta R = 0$ mm. (e) Measured gapped bulk bands for the PC with $\delta R = 1.5$ mm.

the calculated bulk bands in the middle panel of Fig. 1(c) where the two bulk modes are degenerate at 5.02 GHz. This degenerate Dirac point is the singularity which is the source of topological characteristics. By breaking the degeneracy of Dirac point, one can obtain a complete bandgap whose topology is determined by the relation between the intracell and intercell couplings. To see this, we define a parameter $\delta R = R - R_0$ and check the evolution of the two bulk modes. With the increasing of δR, the two bulk modes first come closer, then meet each other, and lastly move apart [Fig. 1(b)] (all simulations are performed with COMSOL MULTIPHYSICS). As shown in the insets of Fig. 1(b), these two bulk modes can be named as monopole-like and dipole-like modes according to their field distributions [43]. When these two different bulk modes switch their positions along the frequency axis, the topological phase transition happens. The topology of the bandgap is determined by the winding number of the first bulk band [44], i.e., $w = (\mathrm{sgn}(t_1 - t_2) - 1)/2$, where t_1 and t_2 are amplitudes of the intracell and intercell couplings. When the intracell coupling is stronger than the intercell coupling (i.e., $t_1 > t_2$), $w = 0$ and the PC is topologically trivial. One example is the PC with $\delta R = -1.5$ mm whose monopole-like mode has a lower frequency than the dipole-like mode [left panel of Fig. 1(c)]. On the other hand, when the intracell coupling is weaker than the intercell coupling (i.e., $t_1 < t_2$), $w = -1$ and the PC is topologically nontrivial. One example is the PC with $\delta R = 1.5$ mm whose dipole-like mode has a lower frequency than the monopole-like mode [right panel of Fig. 1(c)].

Based on the design in Fig. 1 and considering the transverse magnetic (TM) surface wave, we construct a sample that is composed of aluminum rods standing on a flat aluminum surface [Fig. 2(a)]. Between the metallic rods and the metal surface, there is thin poster paper. This paper is drawn with the in-plane pattern for precisely placing all rods. Note that the influence of this paper on the band structures of PC has been considered in our numerical simulation. As the first and second bulk bands locate below the air light line, bulk modes near the Dirac cone can be supported on the surface-wave PC whose surrounding background is the air. To excite bulk modes, the source antenna is inserted through the bottom aluminum surface which is drilled with a hole for the source antenna. To image the E_z field, the probe antenna is placed 1 mm above the top of metallic rods and it is connected to a 2D translation stage for scanning the field within the xy plane from 3.5 to 5.7 GHz. The scan length is $l_x = 450$ mm ($l_y = 290$ mm) with the scanned resolution of $d_x = 1.87$ mm $= a/10$ ($d_y = 1.87$ mm). Figure 2(b) shows the measured field for the PC with $\delta R = 0$ mm at 5 GHz, which does not show the plane wave pattern, indicating that bulk modes with different wave vectors are excited. To check the dominant bulk modes, we perform a fast Fourier transform (FFT) on the measured field and show the obtained experimental eigenfrequency contour for the PC with $\delta R = 0$ mm [Fig. 2(c)]. By repeating the above FFT on the measured fields at all frequencies and sorting out the data at the high-symmetry k-points along the boundary of the Brillouin zone, we can finally get the experimental bulk bands for the PC with $\delta R = 0$ mm [Fig. 2(d)]. The experimental bulk bands are gapless and cross at the K point, showing good agreement with the simulated ones. In addition, we experimentally fabricate the sample with $\delta R = 1.5$ mm and measure its bulk bands [Fig. 2(e)]. The measured gapped bulk bands are also in agreement with the simulated ones, and one complete bandgap is experimentally observed.

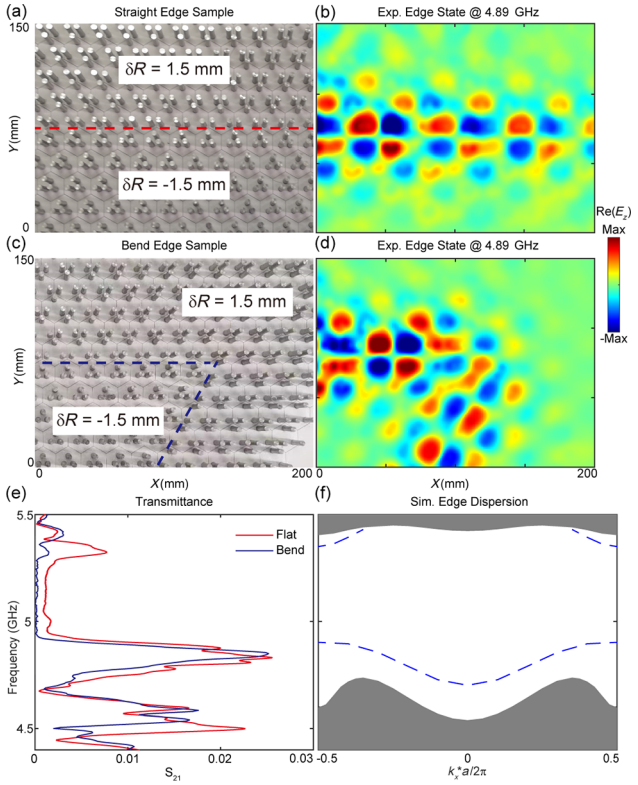

Fig. 3. Observation of robust edge modes. (a) and (c) Photographs of the samples with the straight edge and bend edge, respectively. The boundary is formed by the PC with $\delta R = 1.5$ mm at the top and the PC with $\delta R = -1.5$ mm at the bottom. (b) and (d) Measured E_z fields for two samples at 4.9 GHz for the xy plane which is 1 mm above the top of metallic rods. (e) Measured transmission spectra for two samples. (f) Calculated edge dispersions of the edge presented in (a).

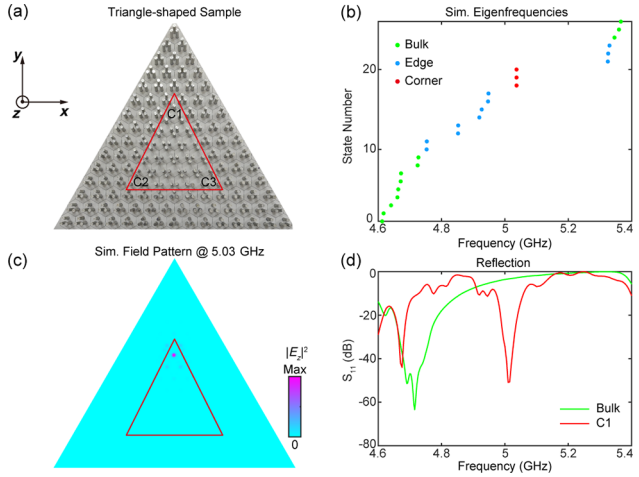

Fig. 4. Observation of in-gap corner mode. (a) Photograph of the triangle-shaped sample which is constructed by surrounding the PC with $\delta R = 1.5$ mm by the PC with $\delta R = -1.5$ mm. Three corners are denoted as C1, C2, and C3. (b) Simulated frequencies of eigenmodes of the sample in (a). There are three in-gap corner modes localizing at three corners. (c) $|E_z|^2$ field of the corner mode with its field localizing at Corner C1. (d) Reflection spectra when the antenna is excited at Corner C1 (red curve) or in the bulk (green curve).

The PCs with $\delta R = 1.5$ mm and $\delta R = -1.5$ mm are topologically distinct and the boundary between them supports robust edge modes. To confirm this, we first construct the straight edge by putting the PC with $\delta R = 1.5$ mm at the top and the PC with $\delta R = -1.5$ mm at the bottom [Fig. 3(a)]. The source is placed at the left end of the sample to excite edge modes, and the probe antenna is once again connected to the translation stage to image the field within the xy plane. For example, the excited edge mode at 4.9 GHz is shown in Fig. 3(b). The edge mode propagates along the x direction, and evanescently decays from the boundary along the y direction. To check the robustness of the edge modes, we then fabricate the sample with a sharp bend [Fig. 3(c)]. The measured E_z field shows that the excited edge mode can turn around the sharp bend and keep propagating forwards. The robust transport of edge modes should apply to edge modes at other frequencies. To see this, we measure the transmission spectra for two waveguides [Fig. 3(e)]. High transmittance is observed in the frequency range from 4.70 to 4.91 GHz which corresponds to the frequency range of edge modes [Fig. 3(f)]. In addition, the transmittances of the two waveguides are nearly the same, confirming the broadband robust transport of edge modes.

Note the edge dispersion in Fig. 3(f) is not gapless. The in-gap corner modes can emerge in the gap of the edge states according to the second-order topology [45]. To see this, we construct a triangle-shaped sample by surrounding the PC with $\delta R = 1.5$ mm by the PC with $\delta R = -1.5$ mm [Fig. 4(a)]. There are three corners, denoted as C1, C2, and C3, which are the same and all support the in-gap corner modes [46]. The numerical eigenmodes of this sample confirm this prediction [Fig. 4(b)]. As expected, besides the bulk modes (green dots) and edge modes (blue dots), three corner modes (red dots) are found at 5.03 GHz within the bandgap. As an example, Fig. 4(c) shows the $|E_z|^2$ field of the corner mode whose distribution is highly localized around Corner C1. To experimentally prove the existence of the corner mode, we measure the reflection spectra by putting the antenna at Corner C1 and inside the bulk [Fig. 4(d)]. When the antenna is placed in the bulk, the reflection coefficient is high within the bulk bandgap because the input source cannot be coupled into the PC and reflected back to the antenna. When the antenna is placed at Corner C1, a reflection dip is found near 5.02 GHz within the bulk bandgap, which is due to the excitation of the corner mode. With the striking comparison between these two reflection spectra, it confirms the existence of the in-gap corner mode.

Note the topological edge states and corner states have been studied in the Kagome dielectric PC [47–49]. There are many differences between the quasi-2D dielectric PC system and surface-wave PC system. Firstly, the parallel-plate waveguide in the quasi-2D dielectric PC largely hampers the probing of fields. In contrast, the cladding-free surface-wave PC enables the direct measurement of surface waves. Secondly, compared with the Kagome dielectric PC which originates from Bragg scattering, the proposed Kagome surface-wave PC originates from local resonance, making it possible to achieve subwavelength field confinement. Thirdly, for the dielectric PC, the modes residing above the light will suffer from leakage into free space if it is not sandwiched between two parallel metallic plates. The modes of surface-wave PC reside below the light line, so that they are tightly confined in the surface of the PC.

In summary, we have extended the topological physics of the Kagome lattice to surface waves and demonstrated a Kagome surface-wave PC. By mapping fields of eigenmodes and using the pump-probe measurement, the gapless and gapped bulk bands, the robust edge modes, and the in-gap corner modes are experimentally confirmed. Our work demonstrates the existence of topological states in a Kagome surface-wave PC and may provide a method to design high-performance photonic devices.

Funding. State Key Research Development Program of China (2022YFA1404304); National Natural Science Foundation of China (12074443, 12204552, 62035016); Basic and Applied Basic Research Foundation of Guangdong Province (2019B151502036, 2023B1515040023); Guangzhou Science, Technology and Innovation Commission (2021020211 57); China Postdoctoral Science Foundation (2022M713641).

Acknowledgments. The authors acknowledge Professor Wen-Jie Chen for helpful discussion.

Disclosures. The authors declare no conflicts of interest.

Data availability. Data underlying the results presented in this paper are not publicly available at this time but may be obtained from the authors upon reasonable request.

REFERENCES

1. H. Kosaka, T. Kawashima, A. Tomita, M. Notomi, T. Tamamura, T. Sato, and S. Kawakami, Appl. Phys. Lett. **74**, 1370 (1999).
2. M. Notomi, Phys. Rev. B **62**, 10696 (2000).
3. C. Luo, S. G. Johnson, J. D. Joannopoulos, and J. B. Pendry, Phys. Rev. B **65**, 201104 (2002).
4. L. Lu, J. D. Joannopoulos, and M. Soljačić, Nat. Photonics **8**, 821 (2014).
5. T. Ozawa, H. M. Price, A. Amo, N. Goldman, M. Hafezi, L. Lu, M. C. Rechtsman, D. Schuster, J. Simon, O. Zilberberg, and I. Carusotto, Rev. Mod. Phys. **91**, 015006 (2019).
6. S. Xia, D. Song, N. Wang, X. Liu, J. Ma, L. Tang, H. Buljan, and Z. Chen, Opt. Mater. Express **11**, 1292 (2021).
7. S. Ma, B. Yang, and S. Zhang, Photonics Insights **1**, R02 (2022).
8. C. He, L. Lin, X.-C. Sun, X.-P. Liu, M.-H. Lu, and Y.-F. Chen, Int. J. Mod. Phys. B **28**, 1441001 (2014).
9. M. Kim, Z. Jacob, and J. Rho, Light: Sci. Appl. **9**, 130 (2020).
10. G. J. Tang, X. T. He, F. L. Shi, J. W. Liu, X. D. Chen, and J. W. Dong, Laser Photonics Rev. **16**, 2100300 (2022).
11. Z. Wang, Y. Chong, J. D. Joannopoulos, and M. Soljačić, Nature **461**, 772 (2009).
12. Y. Poo, R.-x. Wu, Z. Lin, Y. Yang, and C. T. Chan, Phys. Rev. Lett. **106**, 093903 (2011).
13. J. Chen and Z.-Y. Li, Phys. Rev. Lett. **128**, 257401 (2022).
14. A. B. Khanikaev, S. H. Mousavi, W.-K. Tse, M. Kargarian, A. H. MacDonald, and G. Shvets, Nat. Mater. **12**, 233 (2013).
15. W.-J. Chen, S.-J. Jiang, X.-D. Chen, B. Zhu, L. Zhou, J.-W. Dong, and C. T. Chan, Nat. Commun. **5**, 5782 (2014).
16. T. Ma, A. B. Khanikaev, S. H. Mousavi, and G. Shvets, Phys. Rev. Lett. **114**, 127401 (2015).
17. L.-H. Wu and X. Hu, Phys. Rev. Lett. **114**, 223901 (2015).
18. Y. Yang, Y. F. Xu, T. Xu, H.-X. Wang, J.-H. Jiang, X. Hu, and Z. H. Hang, Phys. Rev. Lett. **120**, 217401 (2018).
19. S. Barik, A. Karasahin, C. Flower, T. Cai, H. Miyake, W. DeGottardi, M. Hafezi, and E. Waks, Science **359**, 666 (2018).
20. M. I. Shalaev, W. Walasik, A. Tsukernik, Y. Xu, and N. M. Litchinitser, Nat. Nanotechnol. **14**, 31 (2019).
21. Y. Yang, Y. Yamagami, X. Yu, P. Pitchappa, J. Webber, B. Zhang, M. Fujita, T. Nagatsuma, and R. Singh, Nat. Photonics **14**, 446 (2020).
22. C. W. Peterson, W. A. Benalcazar, T. L. Hughes, and G. Bahl, Nature **555**, 346 (2018).
23. C. W. Peterson, T. Li, W. Jiang, T. L. Hughes, and G. Bahl, Nature **589**, 376 (2021).
24. Y. Liu, S. Leung, F.-F. Li, Z.-K. Lin, X. Tao, Y. Poo, and J.-H. Jiang, Nature **589**, 381 (2021).
25. X.-D. Chen, W.-M. Deng, F.-L. Shi, F.-L. Zhao, M. Chen, and J.-W. Dong, Phys. Rev. Lett. **122**, 233902 (2019).
26. B.-Y. Xie, G.-X. Su, H.-F. Wang, H. Su, X.-P. Shen, P. Zhan, M.-H. Lu, Z.-L. Wang, and Y.-F. Chen, Phys. Rev. Lett. **122**, 233903 (2019).
27. B. Xie, H.-X. Wang, X. Zhang, P. Zhan, J.-H. Jiang, M. Lu, and Y. Chen, Nat. Rev. Phys. **3**, 520 (2021).
28. Y. Ota, F. Liu, R. Katsumi, K. Watanabe, K. Wakabayashi, Y. Arakawa, and S. Iwamoto, Optica **6**, 786 (2019).
29. W. Zhang, X. Xie, H. Hao, J. Dang, S. Xiao, S. Shi, H. Ni, Z. Niu, C. Wang, K. Jin, X. Zhang, and X. Xu, Light: Sci. Appl. **9**, 109 (2020).
30. Z. Gao, L. Wu, F. Gao, Y. Luo, and B. Zhang, Adv. Mater. **30**, 1706683 (2018).
31. S.-H. Kim, S. S. Oh, K.-J. Kim, J.-E. Kim, H. Y. Park, O. Hess, and C.-S. Kee, Phys. Rev. B **91**, 035116 (2015).
32. Z. Gao, H. Xu, F. Gao, Y. Zhang, Y. Luo, and B. Zhang, Phys. Rev. Appl. **9**, 044019 (2018).
33. Z. Gao, F. Gao, and B. Zhang, Appl. Phys. Lett. **108**, 041105 (2016).
34. Y. Zhou, N. Zhang, D. a, J. Bisharat, R. J. Davis, Z. Zhang, J. Friend, P. R. Bandaru, and D. F. Sievenpiper, Phys. Rev. Appl. **19**, 024053 (2023).
35. Z.-D. Zhang, S.-Y. Yu, H. Ge, J.-Q. Wang, H.-F. Wang, K.-F. Liu, T. Wu, C. He, M.-H. Lu, and Y.-F. Chen, Phys. Rev. Appl. **16**, 044008 (2021).
36. D. a, J. Bisharat, and D. F. Sievenpiper, Laser Photonics Rev. **13**, 1900126 (2019).
37. Z. Gao, Z. Yang, F. Gao, H. Xue, Y. Yang, J. Dong, and B. Zhang, Phys. Rev. B **96**, 201402 (2017).
38. L. Zhang, Y. Yang, Z.-K. Lin, P. Qin, Q. Chen, F. Gao, E. Li, J.-H. Jiang, B. Zhang, and H. Chen, Adv. Sci. **7**, 1902724 (2020).
39. X. X. Wu, Y. Meng, J. X. Tian, Y. Z. Huang, H. Xiang, D. Z. Han, and W. J. Wen, Nat. Commun. **8**, 1304 (2017).
40. F. Gao, Z. Gao, X. Shi, Z. Yang, X. Lin, H. Xu, J. D. Joannopoulos, M. Soljacic, H. Chen, L. Lu, Y. Chong, and B. Zhang, Nat. Commun. **7**, 11619 (2016).
41. S. Yves, R. Fleury, T. Berthelot, M. Fink, F. Lemoult, and G. Lerosey, Nat. Commun. **8**, 16023 (2017).
42. J. Guo, B. Yang, S. Ma, H.-C. Chan, G. Situ, and S. Zhang, Laser Photonics Rev. **15**, 2000360 (2021).
43. W.-M. Deng, X.-D. Chen, W.-J. Chen, F.-L. Zhao, and J.-W. Dong, Nanophotonics **8**, 833 (2019).
44. X. Ni, M. A. Gorlach, A. Alu, and A. B. Khanikaev, New J. Phys. **19**, 055002 (2017).
45. X. Ni, M. Weiner, A. Alù, and A. B. Khanikaev, Nat. Mater. **18**, 113 (2019).
46. H. Xue, Y. Yang, F. Gao, Y. Chong, and B. Zhang, Nat. Mater. **18**, 108 (2019).
47. M. Li, D. Zhirihin, M. Gorlach, X. Ni, D. Filonov, A. Slobozhanyuk, A. Alu, and A. B. Khanikaev, Nat. Photonics **14**, 89 (2020).
48. Y. Gong, S. Wong, A. J. Bennett, D. L. Huffaker, and S. S. Oh, ACS Photonics **7**, 2089 (2020).
49. Y.-H. He, Y.-F. Gao, Y. He, X.-F. Qi, J.-Q. Si, M. Yang, and S.-Y. Zhou, Opt. Laser Technol. **161**, 109196 (2023).